第 54 卷第 1 期
2026 年 1 月

硅 酸 盐 学 报
JOURNAL OF THE CHINESE CERAMIC SOCIETY

Vol. 54，No. 1
January，2026

http://jccsoc.cbpt.cnki.net

DOI：10.14062/j.issn.0454-5648.20250215

二(五氟苯基)锌调控无机钙钛矿光伏表面缺陷态密度

王跃霖，王三龙

(东北电力大学电气工程学院，现代电力系统仿真控制与绿色电能新技术教育部重点实验室，吉林 吉林 132012)

摘　要：无机钙钛矿太阳电池(IPSCs)的光和热稳定性良好，是叠层太阳电池(TSCs)优异的顶部电池候选者之一。然而，IPSCs的光吸收层和电子传输层(ETL)之间严重的非辐射复合限制了光电转换效率(PCE)的提升。利用二(五氟苯基)锌(B(PFP)Zn)对光吸收层/ETL 之间的界面缺陷态密度进行调控，B(PFP)Zn 钝化了未配位的铅离子(Pb^{2+})，基于 B(PFP)Zn 空气制备的反式装置的开路电压平均提升约 70 mV。此外，氟化苯基基团的疏水性使得装置耐湿性增强。

关键词：无机钙钛矿太阳电池；二(五氟苯)锌；非辐射复合；缺陷态密度；耐湿性

中图分类号：TQ472.1　　**文献标志码**：A　　**文章编号**：0454–5648(2026)01–0164–07

网络出版时间：2025–11–28

钙钛矿/晶硅叠层太阳电池(TSCs)因其可突破单结晶硅太阳电池的光电转换效率(PCE)在近些年引起了广泛研究[1–4]。一方面，作为 TSCs 顶部电池的有机无机杂化钙钛矿太阳电池(HPSCs)溴元素含量较多，面临着相分离的风险；另一方面，HPSCs 内部的甲基胺(MA)和甲酰胺(FA)在高温下倾向于分解，导致它们的热稳定性差[5–7]。使用无机铯离子(Cs^+)来替代有机成分进行无机钙钛矿太阳电池(IPSCs)的构建是一个极好的解决方案[8–9]。

1.68～1.73 eV 带隙无机钙钛矿的光和热稳定性优异，几乎不存在相分离的风险，是 TSCs 优异的顶部电池候选者之一。自 2023 年报道第 1 篇无机钙钛矿/晶硅两端叠层太阳电池至今，其 PCE 已经由最初的 22.96%提升到 27.27%[10–13]。然而，IPSCs 内部非常严重的非辐射复合限制了单结及 TSCs 装置 PCE 的提升[14–16]。研究表明，钙钛矿太阳电池表面的缺陷态密度较体内高 3 个数量级[17]。因此，合理调控表面缺陷态密度对于提升光伏器件的性能十分必要。

近年来，研究者围绕调控无机钙钛矿的表面缺陷态密度做了系列研究。诸如界面工程[18–20]、维度调控[21–22]、表面重建[23–24]和构建异质结[25–26]等策略被陆续开发出来。IPSCs 的 PCE 也在稳步提升，但多数研究的制备氛围均为惰性氛围，不利于推进 IPSCs 的工业化进程。本工作利用双(五氟苯基)锌(B(PFP)Zn)对光吸收层/ETL 之间的界面缺陷态密度进行管理，经 B(PFP)Zn 处理的装置缺陷态密度由 8.63×10^{15} cm^3 降低到 8.08×10^{15} cm^3。B(PFP)Zn 能与未配位的铅离子(Pb^{2+})相互作用，降低了光吸收层/电子传输层(ETL)界面处的非辐射复合，氟化苯基基团也对离子迁移起到限制作用。基于此，空气制备的反式器件 PCE 由 16.07%显著提升到 18.72%，湿度和热稳定性均有相当程度的提升。

1　实验

1.1　原料

N,N-二甲基甲酰胺(DMF，纯度 99.5%，质量分数，下同)、二甲基亚砜(DMSO，纯度 99.5%)、异丙醇(IPA，纯度 99.5%)、乙醇(EtOH，纯度 99%)、氯苯(CB，纯度 99.5%)购买自 Sigma-Aldrich 公司。碘化铯(CsI，纯度 99.5%)、三碘化氢铅($HPbI_3$，纯度 99.5%)、溴化铅($PbBr_2$，纯度 99.5%)、2,9-二甲基-4,7-联苯-1,10-菲罗啉(BCP，纯度 99.5%)、(2-(9H-咔

收稿日期：2025–03–28。　修订日期：2025–04–28。
基金项目：吉林省自然科学基金–自由探索项目(YDZJ202501ZYTS397)。
第一作者：王跃霖(2002—)，男，硕士研究生。
通信作者：王三龙(1992—)，男，博士，讲师。

Received date: 2025–03–28.　**Revised date:** 2025–04–28.
First author: WANG Yuelin (2002–), male, Master candidate.
E-mail: m15543377302@163.com
Correspondent author: WANG Sanlong (1992–), male, Ph.D., Lecturer.
E-mail: 20233209@neepu.edu.cn

唑-9-基)乙基)膦酸(2PACz，纯度 99%)购自西安宝莱特光电科技有限公司。二(五氟苯基)锌(B(PFP)Zn，纯度 99.7%)购自北京伊诺凯科技有限公司。

1.2　样品制备

铟掺杂氧化锡(In-doped Tin Oxide, ITO)充分清洗干净后，紫外臭氧灯下照射 20 min。随后，将 10.0 mg/mL 的 NiO_x 水溶液，以 2000 r/min 的转速旋涂于臭氧处理后的 ITO 玻璃表面，旋涂时间为 30 s，130 ℃的空气环境中退火 20 min。冷却至室温后，将 1 mg/mL 的 2PACz(EtOH)以 5000 r/min 的转速旋涂于退火后的 NiO_x 表面并 100 ℃退火 10 min。要特别注意的是，2PACz 滴加到 NiO_x 表面后，需要等待其自由扩散开后，静置 10 s 再开始旋涂，有助于 2PACz 和 NiO_x 之间更好的界面接触。按照之前文献报道的方法进行前驱液的配置[27]，于湿度低于 20%的空气环境中以 2000 r/min 的转速旋涂于 70 ℃预热的 2PACz 表面，旋涂时间为 25 s。于 190 ℃的热板上退火约 5～8 min，将退火后的薄膜转移至 N_2 氛围手套箱之中，以 6000 r/min 的转速旋涂 50 μL 浓度为 0.5 mg/mL 的 B(PFP)Zn(IPA)，旋涂时间为 30 s，随后 100 ℃退火 3 min。旋涂 20.0 mg/mL 的 $PC_{61}BM$(CB)作为 ETL，0.5 mg/mL 的 BCP(IPA)旋涂 30 s 作为空穴阻挡层。利用蒸发设备在 BCP 表面蒸发 80.0 nm 的 Ag 作为金属电极。子电池面积为 0.12 cm^2。

1.3　样品表征

利用美国爱丁堡仪器 FLS980 型稳态瞬态荧光磷光光谱仪对参考组和经 B(PFP)Zn 处理的薄膜进行稳态光致发光(PL)和时间分辨光致发光(tTRPL)光谱测试。利用美国 Keithley 2400 型源测量单元仪器在太阳光模拟器发出的 AM 1.5G 光谱下测量器件的 *J*–*V* 特性，光谱的强度通过 KG-5 滤光片的标准硅太阳电池进行校准。使用美国赛默飞 FEI NanoSEM650 型扫描电子显微镜(SEM)测量钙钛矿薄膜表面。利用上海中晨数字技术设备有限公司 POWEREACH JC-2000C1 型接触角测量仪对钙钛矿薄膜的水接触角测量，其波长范围为 300～800 nm。

2　结果与讨论

2.1　无机钙钛矿薄膜的表面特性

利用图 1a 所示的流程图对无机钙钛矿进行制备，无机钙钛矿薄膜的制备过程在空气中进行，湿度控制在 20%以内。B(PFP)Zn/IPA 溶液的界面处理则是在手套箱的氮气氛围下进行，在 B(PFP)Zn 旋涂完成后需要经 100 ℃退火 3 min。从图 1b 可以看出，经过 B(PFP)Zn 处理后的无机钙钛矿对应的(110)、(220)衍射峰增强，半峰宽变窄，半峰宽的变化意味着更大的晶粒直径。这是由于 B(PFP)Zn 在二次退火过程中与无机钙钛矿发生相互作用，实现了再结晶。借助 SEM 对 B(PFP)Zn 处理前后薄膜的

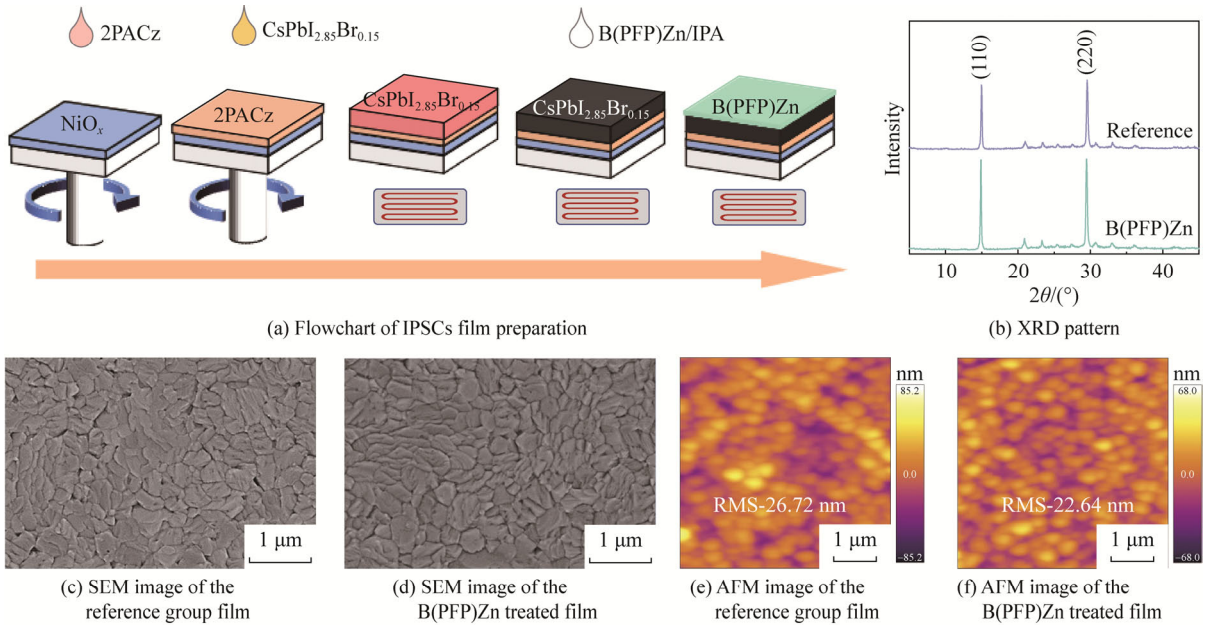


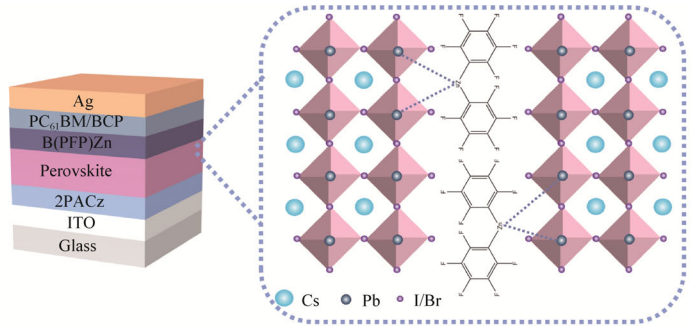
图 1　IPSCs 薄膜制备流程图、XRD 谱、参考组薄膜的 SEM 照片、B(PFP)Zn 处理薄膜的 SEM 照片、参考组薄膜的原子力显微镜 AFM 图像、B(PFP)Zn 处理薄膜的 AFM 图像

Fig. 1　Flowchart of IPSCs film preparation, XRD patterns, SEM image of the reference group film, SEM image of the B(PFP)Zn treated film, AFM image of the reference group film, AFM image of the B(PFP)Zn treated film

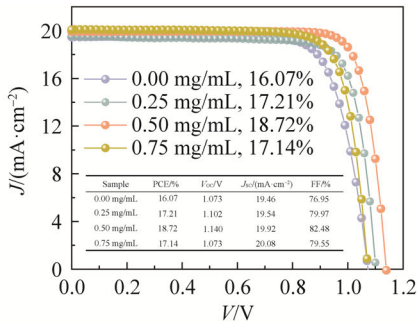
表面形貌进行观测，图 1c 和图 1d 的 SEM 照片表明，经 B(PFP)Zn 处理的薄膜表面孔洞减少，孔洞作为非辐射复合的中心，严重制约着器件的光伏性能[28–29]。如图 1e 和图 1f 所示，参考组薄膜的表面粗糙度为 26.72 nm，而 B(PFP)Zn 处理后薄膜的表面粗糙度仅为 22.64 nm，与 SEM 的结果一致。

2.2 B(PFP)Zn 对 IPSCs 光伏性能的影响

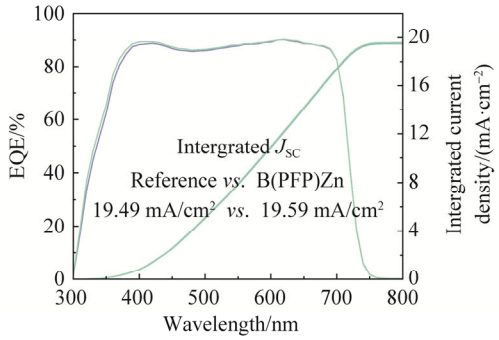
图 2a 左侧为器件结构图。右侧为 B(PFP)Zn 与



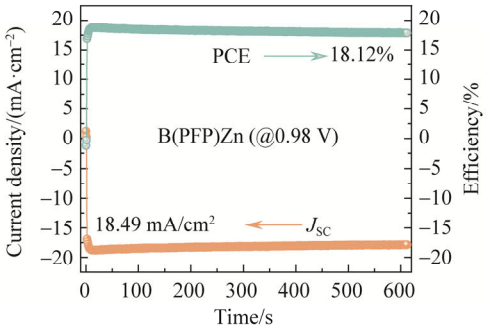
(a) Process flowchart for the preparation of IPSCs and the mechanism diagram of B(PFP)Zn



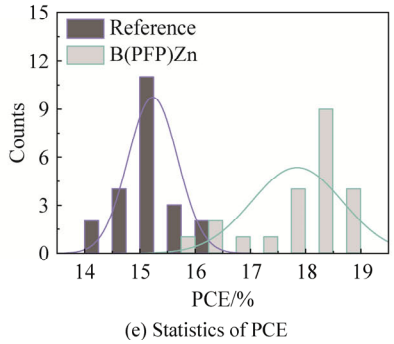
(b) *J*–*V* curves of the champion devices



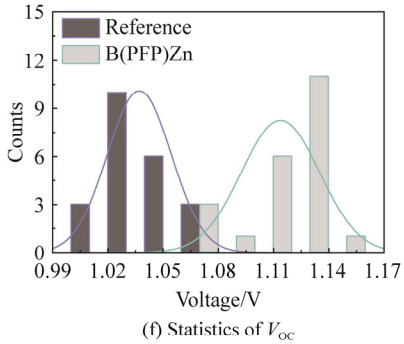
(c) EQE curves



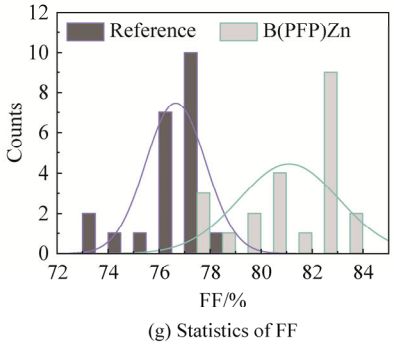
(d) SPO efficiency curves



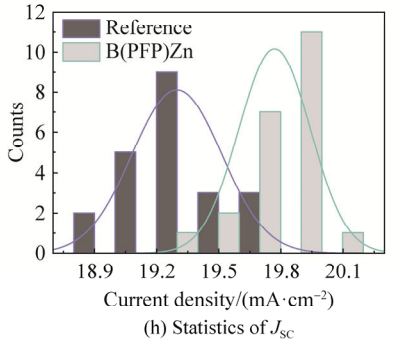
(e) Statistics of PCE



(f) Statistics of V_{OC}



(g) Statistics of FF



(h) Statistics of J_{SC}

图 2 IPSCs 的器件结构示意图及 B(PFP)Zn 的作用机理图、冠军器件的 *J*–*V* 曲线、EQE 曲线、SPO 效率曲线、4 个光伏性能参数的柱状统计分布图 PCE、V_{OC}、FF、J_{SC}

Fig. 2 Process flowchart for the preparation of IPSCs and the mechanism diagram of B(PFP)Zn、*J*–*V* curves of the champion devices、external quantum efficiency (EQE) curves, steady power output (SPO) efficiency curve, the statistics of four photovoltaic performance parameters: photoelectric conversion efficiency (PCE), open circuit voltage (V_{OC}), fill factor (FF) and short-circuit current density (J_{SC})

$CsPbI_{2.85}Br_{0.15}$ 相互作用的机理图。为了讨论添加不同浓度 B(PFP)Zn 对器件性能影响[30]，不同浓度器件的 *J–V* 曲线及其对应参数记录在图 2b 之中，当 B(PFP)Zn 浓度为 0.50 mg/mL 时效果最佳，器件的 *PCE* 由 16.07%显著提升到 18.72%，具体光伏性能参数如图 2b 的插图所示。B(PFP)Zn 处理前后器件的外量子效率(EQE)测试曲线记录在图 2c 中，积分电流密度分别为 19.49 mA/cm^2 和 19.59 mA/cm^2，与 *J–V* 测试中的短路电流密度(J_{SC})匹配良好。冠军装置的稳态输出(SPO)效率曲线如图 2d 所示，600 s 内器件的平均 SPO 效率为 18.12%。利用 B(PFP)Zn 处理后的器件重复性良好。 PCE、V_{OC}、填充因子(FF)和 J_{SC} 4 个光伏性能参数的柱状分布统计数据分别记录在图 2e～图 2h 中，平均 V_{OC} 提升达到 70 mV，平均 FF 由 77%提升到 81%，排除了实验偶然性的影响。

2.3　B(PFP)Zn 提升 IPSCs 光伏性能的机理分析

为探明 B(PFP)Zn 的作用机制，利用 PL 和 TRPL 对薄膜的光学特性进行表征。如图 3a～图 3b 所示，经过 B(PFP)Zn 表面处理后的薄膜具有更高的 PL 强度并且载流子寿命几乎是参考组薄膜的 2 倍，表明钙钛矿/ETL 处的缺陷态密度降低，非辐射复合受到抑制[11]。暗态 *J–V* 测试曲线被记录在图 3c 中，经过 B(PFP)Zn 处理的器件显示出更低的漏电流。利用纯电子器件对 2 种器件进行空间电荷限制电流(SCLC)测试以评估缺陷态密度的变化[31–32]。如图 3d～图 3e 所示(插图为所采取的器件结构图)，经过 B(PFP)Zn 表面处理后，缺陷态密度由 8.63×10^{15} cm^3 降低到 8.08×10^{15} cm^3。此外，通过导纳谱精确量化了不同能量深度缺陷的陷阱密度(tDOS)，如图 3f 所示，B(PFP)Zn 处理薄膜的 tDOS 低于参考组，与 TRPL 图谱和 SCLC 曲线结果一致。进一步证明了 B(PFP)Zn 的引入抑制了非辐射复合，与更高的 V_{OC} 和更优异的光伏性能相对应。

2.4　B(PFP)Zn 对 IPSCs 稳定性的影响

对器件的稳定性进行相关表征。利用水接触角测试仪对 B(PFP)Zn 处理前后薄膜进行测试(图 4a～图 4b)，薄膜的水接触角由参考组的 45.48°增加到 62.82°，增加的水接触角表明疏水特性增强。在 20%～30%的空气环境下对 2 种器件的湿度稳定性进行监测，参考组器件在 115 h 时 PCE 衰减为初始值的 80%，而实验组对应的 PCE 衰减为初始值的 80%的时间约为 300 h，这主要是由于五氟苯基基团的强疏水性在一定程度上阻挡了水分的侵入。在 65 ℃的条件下对 2 种器件的热稳定性进行追踪，500 h 时参考组的 PCE 衰减为初始 PCE 的 59.01%，实验组则可以实现对其初始 PCE 高达 79.83%的保留率。

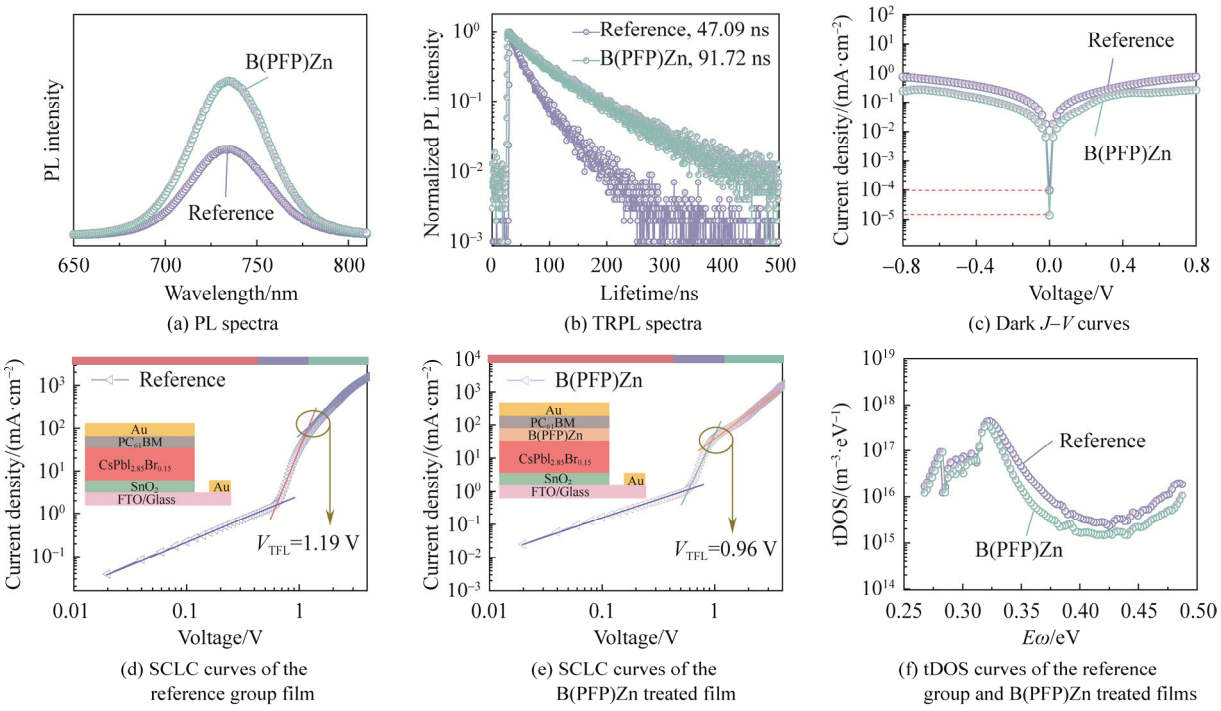
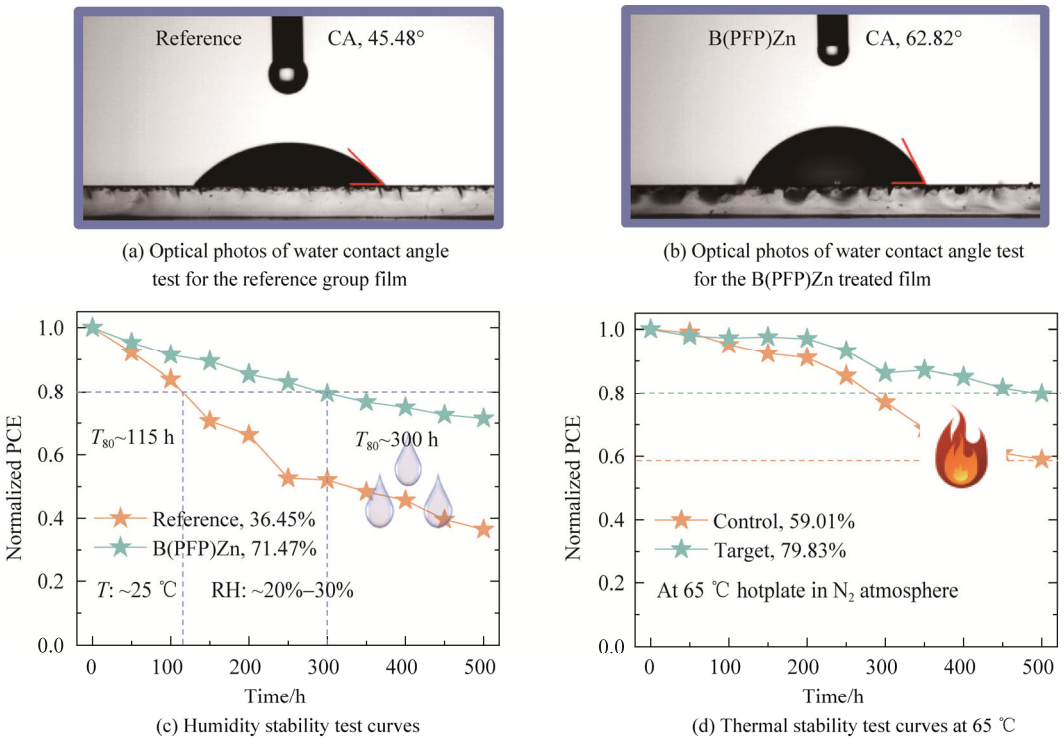


图 3　参考组和 B(PFP)Zn 处理薄膜的 PL 图谱、TRPL 图谱、暗态 *J–V* 曲线、参考组薄膜的 SCLC 曲线、B(PFP)Zn 处理薄膜的 SCLC 曲线、tDOS 曲线

Fig. 3　PL spectra, TRPL spectra, dark *J–V* curves, space charge limited current (SCLC) curves of the reference group film, SCLC curves of the B(PFP)Zn treated film, trap density of states (tDOS) curves of the reference group and B(PFP)Zn treated films



(a) Optical photos of water contact angle test for the reference group film

(b) Optical photos of water contact angle test for the B(PFP)Zn treated film

(c) Humidity stability test curves

(d) Thermal stability test curves at 65 ℃

图 4 参考组薄膜的水接触角测试光学照片、B(PFP)Zn 处理薄膜的水接触角测试光学照片、湿度稳定性测试曲线、65 ℃热稳定性测试曲线

Fig. 4 Optical photos of water contact angle (CA) test for the reference group film, B(PFP)Zn treated film, humidity stability test curves, thermal stability test curves at 65 ℃

3 结论

利用 B(PFP)Zn 对 $CsPbI_{2.85}Br_{0.15}$ 薄膜表面进行后处理，再结晶过程提升了薄膜的结晶质量，有效降低了缺陷态密度，一定程度上抑制了非辐射复合，减少了界面处的载流子积累。基于空气制备的反式 IPSCs 实现了 18.72%的冠军 PCE，平均 V_{OC} 提升高达 70 mV。该策略简单且可重复性高，为光伏产业转型升级提供了科学新思路和技术新路线。

参考文献:

[1] ER-RAJI O, MAHMOUD M A A, FISCHER O, et al. Tailoring perovskite crystallization and interfacial passivation in efficient, fully textured perovskite silicon tandem solar cells[J]. Joule, 2024, 8(10): 2811–2833.

[2] YING Z Q, YANG X, WANG X Z, et al. Towards the 10-year milestone of monolithic perovskite/silicon tandem solar cells[J]. Adv Mater, 2024, 36(37): 2311501.

[3] AYDIN E, UGUR E, YILDIRIM B K, et al. Enhanced optoelectronic coupling for perovskite/silicon tandem solar cells[J]. Nature, 2023, 623(7988): 732–738.

[4] TAO Z W, LU T, GAO X, et al. Heterogeneity of light-induced open-circuit voltage loss in perovskite/Si tandem solar cells[J]. ACS Energy Lett, 2024, 9(4): 1455–1465.

[5] LIU J, AYDIN E, YIN J, et al. 28.2%-efficient, outdoor-stable perovskite/silicon tandem solar cell[J]. Joule, 2021, 5(12): 3169–3186.

[6] SVEINBJÖRNSSON K, LI B, MARIOTTI S, et al. Monolithic perovskite/silicon tandem solar cell with 28.7% efficiency using industrial silicon bottom cells[J]. ACS Energy Lett, 2022, 7(8): 2654–2656.

[7] HAN T J, ZHU W D, WANG T R, et al. MXene-interconnected two-terminal, mechanically-stacked perovskite/silicon tandem solar cell with high efficiency[J]. Adv Funct Mater, 2024, 34(12): 2311679.

[8] WANG S L, GAO J P, CHI K L, et al. Trimming defective perovskite layer surface boosts the efficiency for inorganic solar cells[J]. Appl Surf Sci, 2025, 690: 162654.

[9] JIANG Y, XU T F, DU H Q, et al. Organic-inorganic hybrid nature enables efficient and stable $CsPbI_3$-based perovskite solar cells[J]. Joule, 2023, 7(12): 2905–2922.

[10] WANG S L, WANG P Y, CHEN B B, et al. Suppressed recombination for monolithic inorganic perovskite/silicon tandem solar cells with an approximate efficiency of 23%[J]. eScience, 2022, 2(3): 339–346.

[11] WANG S L, WANG P Y, SHI B, et al. Inorganic perovskite surface reconfiguration for stable inverted solar cells with 20.38% efficiency and its application in tandem devices[J]. Adv Mater, 2023, 35(28): 2300581.

[12] WANG S L, QI S S, SUN H R, et al. Nanoscale local contacts enable inverted inorganic perovskite solar cells with 20.8% efficiency[J]. Angew Chem Int Ed, 2024, 63(19): e202400018.

[13] WANG S L, SUN H R, WANG P Y, et al. Small molecule regulatory strategy for inorganic perovskite solar cells with 368 mV of VOC deficit and its application in tandem devices[J]. Adv Energy Mater, 2024, 14(26): 2400151.

[14] FU S, ZHANG W X, LI X D, et al. Humidity-assisted chlorination with solid protection strategy for efficient air-fabricated inverted

$CsPbI_3$ perovskite solar cells[J]. ACS Energy Lett, 2021, 6(10): 3661–3668.

[15] YANG M, MO K W, ZHU X L, et al. Controlling nucleation and crystallization of $CsPbI_3$ perovskites for efficient inverted solar cells[J]. Small, 2024, 20(28): 2310749.

[16] LU C Y, LI X D, GUO X M, et al. Efficient inverted $CsPbI_3$ perovskite solar cells fabricated in common air[J]. Chem Eng J, 2023, 452: 139495.

[17] NI Z Y, BAO C X, LIU Y, et al. Resolving spatial and energetic distributions of trap states in metal halide perovskite solar cells[J]. Science, 2020, 367(6484): 1352–1358.

[18] FU S, LE J B, GUO X M, et al. Polishing the lead-poor surface for efficient inverted $CsPbI_3$ perovskite solar cells[J]. Adv Mater, 2022, 34(38): 2205066.

[19] LIU N, XU Z X, PAN Y, et al. Efficient inverted CsPbI3 inorganic perovskite solar cells achieved by facile surface treatment with ethanolamine[J]. Chem Commun, 2023, 59(54): 8452–8455.

[20] WANG Z Z, XU T F, LI N, et al. Interfacial engineering with trivalent cations for efficient and stable inverted inorganic perovskite solar cells[J]. Energy Environ Sci, 2024, 17(19): 7271–7280.

[21] TAN S, YU B C, CUI Y Q, et al. Temperature-reliable low-dimensional perovskites passivated black-phase $CsPbI_3$ toward stable and efficient photovoltaics[J]. Angew Chem Int Ed, 2022, 61(23): e202201300.

[22] ZHANG S A, ZHANG L, TIAN Q W, et al. Spontaneous construction of multidimensional heterostructure enables enhanced hole extraction for inorganic perovskite solar cells to exceed 20% efficiency[J]. Adv Energy Mater, 2022, 12(1): 2103007.

[23] CHU X B, YE Q F, WANG Z H, et al. Surface *in situ* reconstruction of inorganic perovskite films enabling long carrier lifetimes and solar cells with 21% efficiency[J]. Nat Energy, 2023, 8(4): 372–380.

[24] TAN C Y, CUI Y Q, ZHANG R, et al. *In situ* reconstructing the buried interface for efficient $CsPbI_3$ perovskite solar cells[J]. ACS Energy Lett, 2025, 10(2): 703–712.

[25] HUANG J, WANG H, CHEN C Y, et al. Ionic bilateral passivator carboxyethylisothiuronium chloride for $CsPbI_{3-x}Br_x$ perovskite solar cells with PCE 20.9% and superior stability[J]. Mater Today, 2023, 67: 46–56.

[26] GUO X M, LU C Y, ZHANG W X, et al. *In situ* surface sulfidation of $CsPbI_3$ for inverted perovskite solar cells[J]. ACS Energy Lett, 2024, 9(1): 329–335.

[27] WANG S L, JIANG H P, GONG Y H, et al. Surface defect clipping strategy enables high-efficiency inorganic perovskite solar cells with ultralow V_{OC} deficit[J]. ACS Sustainable Chem Eng, 2024, 12(42): 15562–15568.

[28] WANG S L, JIANG H P, HAN Z H, et al. Defection-stripping and balanced carrier extraction strategy enables efficient and ultra-low hysteresis of inverted inorganic perovskite solar cells[J]. Chem Eng Sci, 2025, 302: 120891.

[29] LI T X, LI W, WANG K, et al. Ambient air processed inverted inorganic perovskite solar cells with over 21% efficiency enabled by multifunctional ethacridine lactate[J]. Angew Chem Int Ed, 2024, 63(36): e202407508.

[30] XU Y M, ZHANG S Y, YUAN H D, et al. Highly efficient and stable flexible perovskite solar cells enabled by alkylammonium acetate modification with varied dipole moments[J]. Adv Funct Mater, 2025, 35(23): 2422014.

[31] ZHANG B Y, HU Z S, SU J, et al. Inhibiting ion migration and stabilizing crystal-phase in halide perovskite *via* directly incorporated fluoride anion[J]. Angew Chem Int Ed, 2025, 64(1): e202413550.

[32] XU Y M, ZHANG S Y, YUAN H D, et al. Mechanically resilient and highly efficient flexible perovskite solar cells with octylammonium acetate for surface adhesion and stress relief[J]. ACS Nano, 2025, 19(4): 4867–4875.

Effect of Bis(pentafluorophenyl)zinc on Surface Defect State Density in Inorganic Perovskite Photovoltaics

WANG Yuelin, *WANG Sanlong*

(Northeast Electric Power University, Key Laboratory of Modern Power System Simulation Control and New Green Energy Technologies of Ministry of Education, School of Electrical Engineering, Jilin 132012, Jilin, China)

Extended Abstract

Introduction The 1.68–1.73 eV bandgap inorganic perovskite has excellent photovoltaic and thermal stability, and there is almost no risk of phase separation. It is one of the excellent top cell candidates for tandem solar cells (TSCs). However, the extremely serious non-radiative recombination within inorganic perovskite solar cells (IPSCs) severely restricts the improvement of the PCE of single-junction and TSCs devices. Studies have shown that the defect density on the surface of perovskite solar cells is three orders of magnitude higher than that within the material. Therefore, the rational regulation of the defect density on the surface is indispensable for enhancing the performance of photovoltaic devices.

This paper utilizes the dual (pentafluorobenzene) zinc (B(PFP)Zn) to manage the interface defect density between the photoabsorption layer and the ETL. After the B(PFP)Zn treatment, the device defect density has decreased from 1.63×10^{16} cm^3 to 1.32×10^{16} cm^3. Based on this, the PCE of the inverse-type devices fabricated by air was significantly enhanced from 16.07% to 18.72%. Both humidity and thermal stability were improved to a considerable extent.

Results and discussion The diffraction peaks of the inorganic perovskite corresponding to the B(PFP)Zn treatment have been enhanced. This is because B(PFP)Zn interacts with the inorganic perovskite during the secondary annealing process, thereby

achieving recrystallization. Observe the surface morphology of the films before and after B(PFP)Zn treatment by means of SEM. SEM images indicate that the surface pores of the films treated with B(PFP)Zn are reduced. The surface morphology of the film was analyzed by using atomic force microscopy (AFM), the surface roughness of the film treated with B(PFP)Zn was reduced. After the B(PFP)Zn interface treatment, the PCE of the device was significantly enhanced from 16.07% to 18.72%. The average open-circuit voltage (V_{OC}) of the devices increased by 70 mV, and the average FF increased from 77% to 81%.

The films treated by B(PFP)Zn surface treatment have higher PL intensity and the carrier lifetime is nearly twice that of the reference group films, indicating that the defect density at the perovskite/ETL interface has decreased and non-radiative recombination has been suppressed. The devices treated with B(PFP)Zn exhibit lower leakage current. Carry out the space charge limited current (SCLC) tests on the two devices by using the pure hole devices, after the B(PFP)Zn surface treatment, the defect density decreased from 1.63×10^{16} cm^3 to 1.32×10^{16} cm^3.

The humidity stability of the two devices was monitored in an environment with 20% to 30% humidity, the PCE of the reference group devices dropped to 80% of the initial value at 115 h, while that of the experimental group dropped to the same level at approximately 300 h.

Conclusions In this paper, B(PFP)Zn was utilized to perform post-treatment on the surface of $CsPbI_{2.85}Br_{0.15}$ film. The recrystallization process enhanced the crystallization quality of the film, effectively reduced the defect density, to some extent suppressed non-radiative recombination, and decreased the accumulation of charge carriers at the interface. The inverse-phase IPSCs prepared based on air achieved a record PCE of 18.72%, with an average V_{OC} increase of up to 70 mV. This strategy is simple and highly repeatable, providing a new scientific idea and technical route for the transformation and upgrading of the photovoltaic industry.

Keywords inorganic perovskite solar cells; bis(pentafluorobenzene) zinc; non-radiative recombination; defect state density; moisture fastness